Tunable Dielectric Properties of Transition Metal Dichalcogenides

Priya Johari* **and Vivek B. Shenoy***

School of Engineering, Brown University, Providence, Rhode Island 02906, United States

ABSTRACT Since discovery of graphene, layered materials have drawn considerable attention because of their possible exfoliation into single and multilayer 2D sheets. Because of strong surface effects, the properties of these materials vary drastically with the number of layers in a sheet. We have performed first-principles density functional based calculations to evaluate the electron energy loss spectrum (EELS) of bulk, monolayer, and bilayer configurations of several transition metal dichalcogenides, which include semiconducting as well as metallic compounds. Our investigation shows that the peaks in the EELS spectra move toward larger wavelengths (red shift) with the decrease in number of layers. The π plasmon peak shifts slightly by 0.5−1.0 eV, while a significant shift of around 5.5−13.0 eV is obtained for $\pi + \sigma$ plasmon, when exfoliated from bulk to single-layer. This underscores the importance of the interlayer coupling on the loss spectra and the dielectric properties. Our results are found to be in very good agreement with the recent measurements performed by Coleman *et al.* (*Science* 2011, *331*, 568).

KEYWORDS: two-dimensional materials · transition metal dichalcogenides · density functional theory · EELS · plasmon

Layered materials in which quasi two-dimensional sheets are stacked together by weak van der Waals interactions can be used to fabricate low dimensional systems such as zero-dimensional (0D) quantum dots or nanoparticles, one-dimensional (1D) nanoribbons or nanotubes, and two-dimensional (2D) nanosheets. The properties of these low-dimensional systems not only differ from each other but also show distinct behavior with respect to their three-dimensional (3D) counterparts.[1−3] Graphite, one of the best example in this category of layered materials, can be exfoliated into 2D graphene sheets, which exhibit unique electronic, chemical, thermal, and mechanical properties.[4,5] However, zero band gap of graphene limits its use in device application. This has raised interest in exploring other layered materials which can complement graphene's extraordinary properties and can also be used to develop electronic and optical nanodevices.[6]

Recently, the monolayer of MoS_2 has attracted attention for its application in electronics, in particular as field effect transistors (FETs).[6] MoS_2 belongs to the family of transition metal dichalcogenides (TMDs) which exhibit layer-type structure, similar to graphite. TMDs can be metallic, semimetallic, or semiconducting depending on their chemical composition and how their atoms are arranged,[7,8] and can potentially find a wide range of applications in the field of nanoelectronics. Transition metal dichalcogenides are inorganic compounds with chemical formula MX_2, where M stands for transition metal (e.g., M = Mo, W, Ta, Nb, Ni) and X for chalcogenides (X = S, Se, or Te). They generally possess a "sandwich" type of structure in which metal atoms are located in between two layers of chalcogen atoms (see Figure 1). Atoms within these three layers are bonded covalently, while individual sheets are bound *via* weak van der Waals interaction, which makes properties of these materials extremely anisotropic. Like graphene, single sheets of TMDs can be extracted from the bulk using mechanical or solvent-based-exfoliation methods.[3,6,9,10]

To realize the use of thin 2D sheets of layered materials for commercial production, large and uniform sheets are required. However to identify the number of layers in a sheet, analysis tools like transmission electron microscopy (TEM), coupled with flake-edge analysis, electron diffraction, or/and electron energy loss spectroscopy (EELS) can be used.[10,11] Among these techniques, EELS is considered to be a powerful technique which correlates the atomic and electronic structure.[11] Moreover, since the electronic and dielectric properties of layered materials change when exfoliated from bulk, study of EELS spectra can be a useful tool to investigate the change in properties of these compounds with respect to number of layers.

The EELS spectra of many of the crystalline TMDs have already been studied;[10,12−14] however, variation in the EELS spectrum with respect to the number of layers in exfoliated sheets has only been studied recently by Coleman *et al.*[10] They developed a method of liquid-exfoliation of layered materials, which is insensitive to air and water content

* Address correspondence to priya_johari@brown.edu, vivek_shenoy@brown.edu.

Received for review May 9, 2011 and accepted June 27, 2011.

Published online June 27, 2011
10.1021/nn201698t

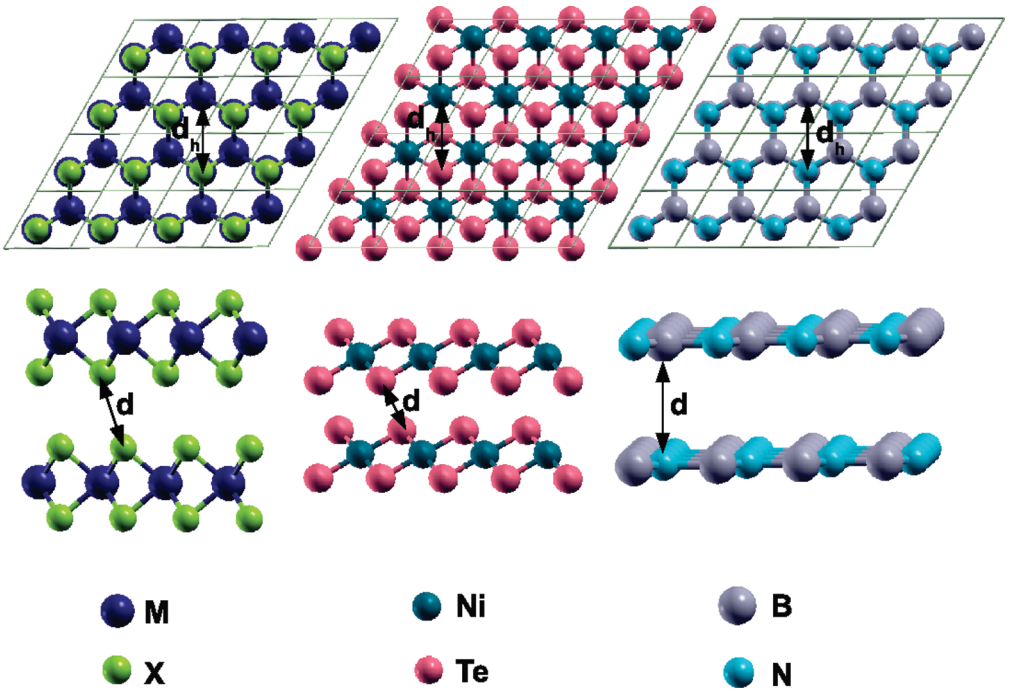

Figure 1. Top (upper panel) and side view (lower panel) of structures of transition metal dichalcogenides (MX_2) of trigonal (left) and octahedral coordination (middle), and *h*-BN (right).

and can generate large quantities of exfoliated material. Coleman *et al.* used low-loss EELS measurements to show the presence of monolayers in a few of their samples (*e.g.*, *h*-BN, MoS_2, and $MoSe_2$).[10] To the best of our knowledge, no theoretical study has been carried out to study the variation in the dielectric response with respect to the number of layers in TMDs. Therefore, in this work, we present the low-loss EELS of monolayer, bilayer, and bulk configurations of several semiconducting (MoS_2, $MoSe_2$, $MoTe_2$, WS_2, WSe_2, WTe_2) and metallic (TaS_2, $TaSe_2$, $TaTe_2$, NbS_2, $NbSe_2$, $NbTe_2$, and $NiTe_2$) TMDs. Moreover, to examine a general impact of film thickness on the dielectric properties of layered materials of various natures, we also studied EELS of insulating *h*-BN, to compare and contrast with the spectra of semiconducting and metallic TMDs.

RESULTS AND DISCUSSION

The structures of the materials we have considered, TMDs (MoS_2, $MoSe_2$, $MoTe_2$, WS_2, WSe_2, WTe_2, NbS_2, $NbSe_2$, $NbTe_2$, TaS_2, $TaSe_2$, $TaTe_2$) with trigonal prismatic coordination, $NiTe_2$ with octahedral coordination, and *h*-BN are shown in Figure 1.[13] In all structures, atoms in a layer are arranged such that they form a hexagonal ring of width d_h. The interlayer spacing in *h*-BN and the shortest X−X distance between two layers in the case of TMDs is denoted by "d". In *h*-BN, layers follow AA stacking, in $NiTe_2$ they are arranged in ABA stacking, while in other TMDs they are piled up in ABABAB type of stacking.

We first performed ground state calculations by relaxing atoms as well as lattice vectors of each system.

TABLE 1. The Optimized Structural Parameters of Crystalline Structures of Several TMDs and *h*-BN[a]

system	*a* (Å)	*c*/*a* (Å)	BL (Å)	d_h (Å)	*d* (Å)
MoS_2	3.1827	2 × 2.1737	2.41	3.99	4.21
$MoSe_2$	3.3182	2 × 2.2047	2.54	4.18	4.41
$MoTe_2$	3.5524	2 × 2.1049	2.73	4.48	4.38
WS_2	3.1823	2 × 2.1797	2.41	3.99	4.21
WSe_2	3.3171	2 × 2.2499	2.54	4.18	4.53
WTe_2	3.5496	2 × 2.1015	2.73	4.48	4.34
NbS_2	3.3553	2 × 2.0084	2.49	4.18	4.09
$NbSe_2$	3.4805	2 × 1.9915	2.62	4.36	4.09
$NbTe_2$	3.6952	2 × 1.9505	2.82	4.65	4.11
TaS_2	3.3354	2 × 2.0689	2.48	4.15	4.24
$TaSe_2$	3.4669	2 × 2.0348	2.61	4.34	4.21
$TaTe_2$	3.6930	2 × 1.9804	2.81	4.64	4.23
$NiTe_2$	3.8937	1.3599	2.60	4.68	3.50
h-BN	2.5046	2.5949	1.45	2.89	3.25

[a] Lattice vector along *x*-direction (*a*), ratio between the lattice vectors in *z*- and *x*-direction (*c*/*a*), bond length between M and X atoms (B and N atoms in the case of *h*-BN) (BL), hexagonal width (d_h), shortest X−X interlayer distance (*d*) (interlayer spacing in *h*-BN) of crystalline structure of several TMDs and *h*-BN.

Table 1 presents the optimized structural parameters such as in-plane lattice vector *a*, ratio between the lattice vectors in *z*- and *x*-direction (*c*/*a*), bond length (BL), d_h, and *d* for all systems. Our calculations found the hexagonal width of MoS_2 to be 3.99 Å (see Table 1), which slightly overestimates the experimental value of 3.80 Å, while the hexagonal width of WS_2 is obtained to be in perfect agreement with the measured results.[10] Our results for other TMDs and *h*-BN also agree well with the experimental and other available crystallographic

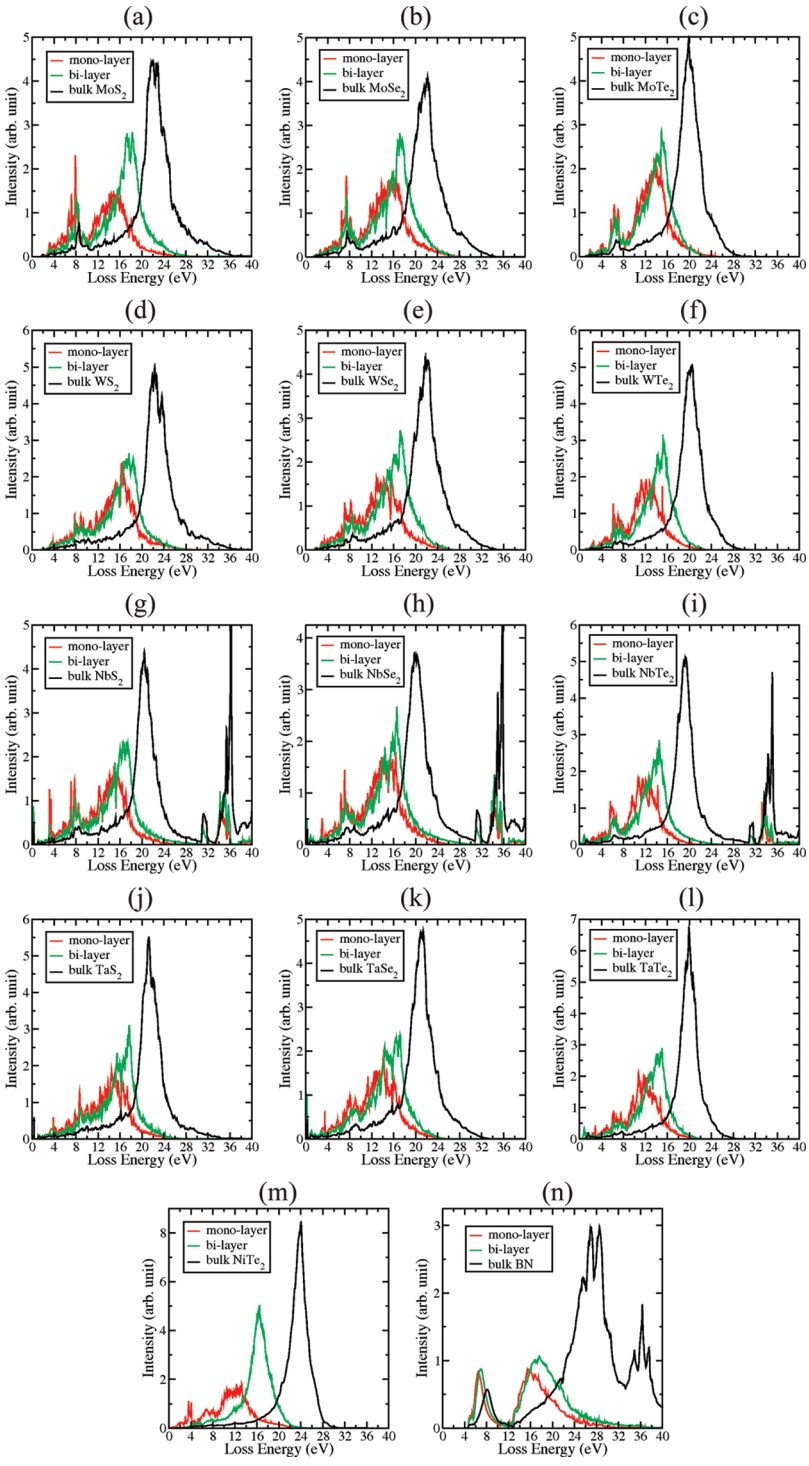

Figure 2. The electron energy-loss spectra of monolayer (red), bilayer (green), and bulk (black) configurations of (a) MoS_2, (b) $MoSe_2$, (c) $MoTe_2$, (d) WS_2, (e) WSe_2, (f) WTe_2, (g) NbS_2, (h) $NbSe_2$, (i) $NbTe_2$, (j) TaS_2, (k) $TaSe_2$, (l) $TaTe_2$, (m) $NiTe_2$, and (n) *h*-BN.

data.[8,10,15,16] We note that lattice parameters for dichalcogenides of the same group of transition metals are almost the same. For example, lattice vectors *a* and *c*, M−X bond length and d_h of VI group transition metal disulfides (MoS_2 and WS_2) and V group transition metal diselenides ($NbSe_2$ and $TaSe_2$) are almost the same (see Table 1). This lattice match provides a suitable platform to prepare hybrid films with varying properties.

Next we calculated electron energy-loss spectra (EELS) for bulk, monolayer, and bilayer configurations of each system to evaluate the dependence of dielectric response on the number of layers. The EELS spectra of single, bilayer, and bulk (red, green, and black) are presented together in Figure 2. All spectra are computed considering in-plane momentum, that is, when the scattering vector **q** is parallel to the basal plane (**q**||**a**).

TABLE 2. The π and $\pi + \sigma$ Plasmon Peak Positions of Monolayer, Bilayer, And Bulk Configurations of Various Layered Materials, Obtained from EELS Spectra Depicted in Figure 2. For Comparison, Available Experimental Values Are Also Given in Parentheses

	π plasmon peak (eV)			$\pi + \sigma$ plasmon peak (eV)		
System	monolayer	bilayer	bulk	monolayer	bilayer	bulk
MoS_2	7.6 (6.5[10])	7.8	8.5 (8.5,[10] 8.9,[13] 8.0[12])	15.6 (20.0)	17.9	22.1 (23.5,[10] 23.4,[13] 23.0[12,14])
$MoSe_2$	7.0	7.3	7.8 (8.0[13])	14.9	17.2	21.3 (22.0[13])
$MoTe_2$	6.3	6.6	6.8	14.3	15.2	19.8
WS_2				15.2 (15.0[10])	16.4	22.3 (23.0,[10] 23.4[13])
WSe_2				14.1	16.2	21.6 (22.2[13])
WTe_2				12.4	14.6	20.2
NbS_2	7.7	7.8	8.3 (8.7[13])	14.0	15.6	20.4 (22.3[13])
$NbSe_2$	7.0	7.6	8.1 (7.7[13])	13.8	15.4	20.0 (21.0[13])
$NbTe_2$	6.0	6.2	6.5	11.7	13.4	19.2
TaS_2				14.4	16.4	21.1 (21.9[13])
$TaSe_2$				13.8	14.9	20.7 (21.0[13])
$TaTe_2$				11.9	14.0	19.8
$NiTe_2$				10.2	16.1	23.6
h-BN	6.5 (6.5[10])	6.9	8.1 (8.5[10,17])	15.4 (15.5[10])	16.6	26.1 (26.5,[10] 26.4[17])

From Figure 2, we can see that all spectra consist of two prominent resonance features that lie (i) below 9 eV (called the π plasmon peak) and (ii) above 9 eV (the $\pi + \sigma$ plasmon peak). The π plasmon feature arises due to collective $\pi-\pi^*$ transition, while $\pi + \sigma$ plasmon results from the $\pi-\sigma^*$ and $\sigma-\sigma^*$ excitations.[14] In MX_2, 12 electrons per molecule constitute the σ valence band, while 5, 6, and 10 electrons in V, VI, and X group TMDs, respectively, form the π plasmon band.[13]

Our calculated π and $\pi + \sigma$ plasmon peak energy locations for bulk, monolayer, and bilayer TMDs and *h*-BN are presented in Table 2. Available experimental values are also given in parentheses for the sake of comparison. On analyzing the data presented in Table 2, we find that our results for bulk phase are in excellent quantitative agreement with the recent EELS measurements performed by Coleman *et al.*,[10] as well as the pioneering work of Liang and Cundy.[13] On examining the graphs presented in Figure 2 we find that spectra of *h*-BN and 4d TMDs (MoX_2 and NbX_2) exhibit two specific features corresponding to π and $\pi + \sigma$ plasmons, while in 5d materials, WX_2 and TaX_2, the π plasmon peak is relatively not well-defined. Moreover, the lower energy plasmon loss peak (π) is found to be little broader in group V material (NbX_2) as compared to the group VI MoX_2. These findings are well supported by experiments.[10,13] The former diffuse behavior of π plasmon feature in 5d TMDs is attributed to the increase in the overlap of the π and σ valence bands, because of the increase of the bandwidth in heavier systems, while the overlap between valence bands is due to the half filled d_{z2} band in the group V compound. In the spectra of NbX_2 (see Figure 2g−i), besides the two main features (π and $\pi + \sigma$), a few other peaks at higher loss energy are obtained. These peaks probably arise due to atomic-like excitations from core d electrons of Nb.[13]

The main goal behind the present work is to examine the variation in EELS of layered materials with respect to the number of layers. On analyzing the EELS spectra for semiconducting MoS_2 our results show a displacement of the π ($\pi + \sigma$) plasmon peak from 8.5 eV (22.1 eV) to 7.6 eV (15.6 eV) for the case of bulk and single-layer, respectively. In semiconducting WS_2 and metallic TaS_2, the $\pi + \sigma$ plasmon of the bulk system is obtained at approximately 22 and 21 eV, respectively, which moves toward lower energy by roughly 7 eV in the case of the monolayer. We find that EELS is not only a useful tool to distinguish a thick slab (bulk) from a thin slab (monolayer), but it can also differentiate a bilayer from a monolayer. It is evident from Figure 2 and Table 2 that even on the variation of slab thickness from two to one layer, the loss spectra shift toward lower energies. For example, in case of MoS_2, the π plasmon peak shifts slightly by 0.3 eV, while a prominent red shift can be seen in the $\pi + \sigma$ plasmon peak, which moves by 2.3 eV, when slab thickness changes from two layers to one layer. Moreover, the intensity of the plasmon peaks also varies with the change in number of layers (see Figure 2). The intensity of the π plasmon peak increases, while that of $\pi + \sigma$ plasmon decreases with a decrease in the number of layers. However, peak intensities in experiments depend on a number of factors, in particular the lateral size of monolayer and bilayer or bulk samples, so a direct comparison of computed intensities is not possible. We observe similar trends of the red shift of EELS spectra and the reduction in the intensity of the $\pi + \sigma$ plasmon for the thin slabs (bilayer and monolayer) of other semiconducting and metallic TMDs, as well as insulating *h*-BN (see Table 2). In case of bulk *h*-BN (see Figure 2n and Table 2), we find π and $\pi + \sigma$

plasmons at around 8.1 and 26.1 eV, respectively, which subsequently shift to 6.5 eV (6.9) eV and 15.4 eV (16.6 eV) in the case of the monolayer (bilayer). Thus, a red shift in the EELS of layered materials can be seen with the decrease in number of layers, regardless of the metallic, semiconducting, or insulating nature of the material. The π plasmon peak moves slightly by around 0.5−1.0 eV, while $\pi + \sigma$ plasmon shows a huge displacement of roughly 5.5−13.0 eV. The reason behind the shift in plasmon loss spectrum with respect to the number of layers can be understood by looking at eqs 1 and 2. The plasmon resonance in solids is described by a maximum in the loss energy function (see eq 1), which depends on the dielectric function. Thus, the plasmon resonance frequency and intensity directly depends on parameters like number of conduction and valence bands, *k*-points, and the volume of the unit cell, Ω, which in turn depends some what on the slab thickness. The bulk systems possess smaller volume per unit cell, larger electron screening, and denser *k*-point mesh as compared to the slab configurations. Also, the different interlayer stacking in the layered compounds increases the number of atoms, and thus the number of bands, in bulk or thick layered systems (bilayer or so) as compared to the monolayer. Our results agree very well with the experimental findings,[10] and reveal a strong sensitivity of energy loss spectra to the number of layers in the structure, and the highly anisotropic aspect of layered materials. The large difference in the spectra of the bulk and the single-layer illustrates the obvious influence of surface effects and the loss of bulk characteristics in the case of the monolayer configuration.

CONCLUSIONS

To study the influence of layer thickness we have studied the dielectric properties of single-layer, bilayer, and bulk TMDs and *h*-BN by computing the EELS spectra using first principles calculations. The calculations were performed on materials with insulating, semiconducting, and metallic behavior. We found that in all the cases we considered, the spectrum considerably shifts toward lower energy when exfoliated from bulk to single-layers. Subsequently, a distinct reduction in the intensity of the bulk $\pi + \sigma$ plasmon and increment in the surface π plasmon intensity is also observed with the decrease in the number of layers. This effect is very similar to the one observed in the well-studied case of graphene.[18,19] This explains that the shift in the loss spectrum of the layered materials with the number of layers is independent of the metallic or semiconducting nature of the material. Our results are found to be in excellent agreement with experiments. They elucidate the role of interlayer coupling in determining the loss spectra of layered material, which vary substantially with the number of layers, and thereby, allow for the determination of layer thickness by studying the loss spectra.

COMPUTATIONAL DETAILS

EELS of TMDs and *h*-BN are calculated using the first principles density functional theory (DFT), as implemented in the Vienna *ab Initio* Simulation (VASP) Package.[20,21] Projector-augmented-wave (PAW) potentials[22] are used to mimic the ionic cores, while the generalized gradient approximation (GGA) in the Perdew−Burke−Ernzerhof[23] (PBE) flavor is employed for the exchange and correlation functional. Atomic positions, as well as lattice vectors are optimized using a conjugate gradient algorithm. Ionic and electronic relaxation is performed by applying a convergence criteria of 10^{-2} eV/Å and 10^{-4} eV, respectively. A *k*-point sampling of 35 × 35 × 35 is used for the relaxation and DOS calculations, while a smaller *k*-mesh of 25 × 25 × 25 is considered for the EELS calculations of bulk. Calculations for slabs (monolayer and bilayer) are performed using a single *k*-point in the *z*-direction. A plane wave cutoff of 400 eV is used in all calculations, while a vacuum of around six layers is used for the calculations of monolayer and bilayer configurations, to avoid interaction between periodic images of slabs in *z*-direction.

The low-loss electron energy-loss spectrum (EELS) is calculated in the long-wavelength limit $q \rightarrow 0$, which essentially determines the optical properties in the wavelength regime accessible to optical or electronic probes. VASP calculates the imaginary part of frequency dependent dielectric tensor ($\varepsilon_{\alpha\beta}^{(2)}$) using the following expression:

$$\varepsilon_{\alpha\beta}^{(2)}(\omega) = \frac{4\pi^2 e^2}{\Omega} \lim_{q\rightarrow 0} \frac{1}{q^2} \sum_{c,v,\mathbf{k}} 2w_k \delta(\varepsilon_{c\mathbf{k}} - \varepsilon_{v\mathbf{k}} - \omega) \times \langle u_{c\mathbf{k}+e_\alpha q} | u_{v\mathbf{k}} \rangle \langle u_{c\mathbf{k}+e_\beta q} | u_{v\mathbf{k}} \rangle^* \quad (1)$$

and then uses the Kramers−Kronig transformation to obtain its real part ($\varepsilon_{\alpha\beta}^{(1)}$).[24,25] In the above expression, indices *c* and *v* refer to the conduction and the valence band states, respectively, $u_{\mathbf{k}}$ is an eigenstate with wave vector $\mathbf{k}$, $w_{\mathbf{k}}$ are the *k*-point weights, which are defined such that they sum to 1, the factor 2 before the weights accounts for the fact that a spin-degenerate system is considered, and Ω is the volume of the unit cell. The vectors e_α are the unit vectors for the three Cartesian directions. Note that the frequency ω has the dimensions of an energy. The loss spectra are computed by taking the imaginary part of the inverse of the frequency dependent microscopic dielectric tensor ($\varepsilon_{\alpha\beta}$) in the random phase approximation (RPA); that is,

$$\begin{aligned} \text{loss energy}\ (\omega) &= \text{Im}\left(\frac{-1}{\varepsilon_{\alpha\beta}(\omega)}\right) \\ &= \text{Im}\left(\frac{-1}{\varepsilon_{\alpha\beta}^{(1)}(\omega) + \iota\varepsilon_{\alpha\beta}^{(2)}(\omega)}\right) \\ &= \frac{\varepsilon_{\alpha\beta}^{(2)}(\omega)}{\varepsilon_{\alpha\beta}^{(1)2}(\omega) + \varepsilon_{\alpha\beta}^{(2)2}(\omega)} \end{aligned} \quad (2)$$

The RPA approximation accounts for the weak screened Coulomb interaction to describe the dynamic linear electronic response of plasmons at the mean-field level, and thus, our calculations miss the many-body effects. However, the agreement

of our previous EELS calculations[11] with the experimental spectra[11,18] suggests that these effects may not be crucial.

Acknowledgment. The support of the Army Research Office through Contract W911NF-11-1-0171 is gratefully acknowledged. Computational support for this research was provided by Grants TG-PHY100022 and TG-DMR090098 from the TeraGrid advanced support program, and the Center for Computation and Visualization at Brown University.

REFERENCES AND NOTES

1. Park, H.; Park, J.; Lim, A. K. L.; Anderson, E. H.; Alivisatos, A. P.; McEuen, P. L. Nanomechanical Oscillations in a Single-C-60 Transistor. *Nature* **2000**, *407*, 57–60.
2. Yanson, A. I.; Bollinger, G. R.; van den Brom, H. E.; Agrait, N.; van Ruitenbeek, J. M. Formation and Manipulation of a Metallic Wire of Single Gold Atoms. *Nature* **1998**, *395*, 783–785.
3. Lee, C.; Li, Q. Y.; Kalb, W.; Liu, X. Z.; Berger, H.; Carpick, R. W.; Hone, J. Frictional Characteristics of Atomically Thin Sheets. *Science* **2010**, *328*, 76–80.
4. Novoselov, K. S.; Geim, A. K.; Morozov, S. V.; Jiang, D.; Zhang, Y.; Dubonos, S. V.; Grigorieva, I. V.; Firsov, A. A. Electric Field Effect in Atomically Thin Carbon Films. *Science* **2004**, *306*, 666–669.
5. Geim, A. K. Graphene: Status and Prospects. *Science* **2009**, *324*, 1530–1534.
6. Radisavljevic, B.; Radenovic, A.; Brivio, J.; Giacometti, V.; Kis, A. Single-layer MoS_2 transistors. *Nat. Nanotechnol.* **2011**, *6*, 147–150.
7. Marseglia, E. A. Transition Metal Dichalcogenides and Their Intercalates. *Int. Rev. Phys. Chem.* **1983**, *3*, 177–216.
8. Wilson, J. A.; Yoffe, A. D. The Transition Metal Dichalcogenides Discussion and Interpretation of the Observed Optical, Electrical and Structural Properties. *Adv. Phys.* **1969**, *18*, 193–335.
9. Benameur, M. M.; Radisavljevic, B.; Heron, J. S.; Sahoo, S.; Berger, H.; Kis, A. Visibility of dichalcogenide nanolayers. *Nanotechnology* **2011**, *22*, 125706.
10. Coleman, J. N.; Lotya, M.; O'Neill, A.; Bergin, S. D.; King, P. J.; Khan, U.; Young, K.; Gaucher, A.; De, S.; Smith, R. J.; Shvets, I. V.; Arora, S. K.; Stanton, G.; Kim, H. Y.; Lee, K.; *et al.* Two-Dimensional Nanosheets Produced by Liquid Exfoliation of Layered Materials. *Science* **2011**, *331*, 568–571.
11. Sun, J. B.; Hannon, J. B.; Tromp, R. M.; Johari, P.; Bol, A. A.; Shenoy, V. B.; Pohl, K. Spatially-Resolved Structure and Electronic Properties of Graphene on Polycrystalline Ni. *ACS Nano* **2010**, *4*, 7073–7077.
12. Disko, M. M.; Treacy, M. M. J.; Rice, S. B.; Chianelli, R. R.; Gland, J. A.; Halbert, T. R.; Ruppert, A. F. Spatially resolved electron energy-loss spectroscopy of MoS_2 platelets. *Ultramicroscopy* **1987**, *23*, 313–319.
13. Liang, W. Y.; Cundy, S. L. Electron Energy Loss Studies of the Transition Metal Dichalcogenides. *Philos. Mag.* **1969**, *19*, 1031–1043.
14. Zeppenfeld, K. Electron Energy Losses and Optical Anisotropy of MoS_2 Single Crystal. *Opt. Commun.* **1970**, *1*, 377–378.
15. Dawson, W. G.; Bullet, D. W. Electronic Structure and Crystallography of $MoTe_2$ and WTe_2. *J. Phys. C* **1987**, *20*, 6159–6174.
16. Bensch, W.; Heid, W.; Muhler, M.; Jobic, S.; Brec, R.; Rouxel, J. Anionic Polymeric Bonds in Nickel Ditelluride: Crystal Structure, and Experimental and Theoretical Band Structure. *J. Solid State Chem.* **1996**, *121*, 87–94.
17. Tarrio, C.; Schnatterly, S. E. Interband-Transitions, Plasmons, and Dispersion in Hexagonal Boron-Nitride. *Phys. Rev. B* **1989**, *40*, 7852–7859.
18. Eberlein, T.; Bangert, U.; Nair, R. R.; Jones, R.; Gass, M.; Bleloch, A. L.; Novoselov, K. S.; Geim, A.; Briddon, P. R. Plasmon Spectroscopy of Free-Standing Graphene Films. *Phys. Rev. B* **2008**, *77*, 233406.
19. Gass, M. H.; Bangert, U.; Bleloch, A. L.; Wang, P.; Nair, R. R.; Geim, A. K. Free-Standing Graphene at Atomic Resolution. *Nat. Nanotechnol.* **2008**, *3*, 676–681.
20. Kresse, G.; Furthmuller, J. Efficient Iterative Schemes for *ab Initio* Total-Energy Calculations Using a Plane-Wave Basis Set. *Phys. Rev. B* **1996**, *54*, 11169–11186.
21. Kresse, G.; Furthmuller, J. Efficiency of *ab-Initio* Total Energy Calculations for Metals and Semiconductors Using a Plane-Wave Basis Set. *Comput. Mater. Sci.* **1996**, *6*, 15–50.
22. Kresse, G.; Joubert, D. From Ultrasoft Pseudopotentials to the Projector Augmented-Wave Method. *Phys. Rev. B* **1999**, *59*, 1758–1775.
23. Perdew, J. P.; Burke, K.; Ernzerhof, M. Generalized Gradient Approximation Made Simple. *Phys. Rev. Lett.* **1996**, *77*, 3865–3868.
24. Gajdos, M.; Hummer, K.; Kresse, G.; Furthmuller, J.; Bechstedt, F. Linear Optical Properties in the Projector-Augmented Wave Methodology. *Phys. Rev. B* **2006**, *73*, 045112.
25. Ehrenreich, H.; Cohen, M. H. Self-Consistent Field Approach to the Many-Electron Problem. *Phys. Rev.* **1959**, *115*, 786–790.